



ELSEVIER

Comput. Methods Appl. Mech. Engrg. 191 (2002) 2179–2189

**Computer methods
in applied
mechanics and
engineering**

www.elsevier.com/locate/cma

Hysteresis in flow past a NACA 0012 airfoil

Sanjay Mittal*, Priyank Saxena

Department of Aerospace Engineering, Indian Institute of Technology, Kanpur, UP 208 016, India

Received 20 February 2001

Abstract

Computations for two-dimensional flow past a stationary NACA 0012 airfoil are carried out with progressively increasing and decreasing angles of attack. The incompressible, Reynolds averaged Navier–Stokes equations in conjunction with the Baldwin–Lomax model, for turbulence closure, are solved using stabilized finite element formulations. Beyond a certain angle of attack the flow stalls with a sudden loss of lift and increase in drag. Hysteresis in the aerodynamic coefficients is observed for a small range of angles of attack close to the stall angle. This is caused by the difference in the location of the separation point of the flow on the upper surface of the airfoil during the increasing and decreasing angles of attack. With the increasing angle, the separation point moves gradually towards the leading edge. With the decreasing angle, the movement of the separation point away from the leading edge is abrupt. © 2002 Elsevier Science B.V. All rights reserved.

Keywords: Turbulent flow; Stall; Airfoil; Hysteresis; Finite elements

1. Introduction

As the angle of incidence of an airfoil to the oncoming flow increases beyond a certain point, stall is observed. The massive flow separation on the airfoil surface results in a sharp drop in lift and increase in the drag. In certain cases, the stall is accompanied by a *hysteresis* in the flow. While the hysteresis associated with the pitching motion of airfoil (also known as dynamic stall) has been investigated quite extensively (see, for example, [9]), the one observed for static stall has received much less attention.

Hoffmann [5] has reported his results for an experimental study for flow past a NACA 0015 airfoil at $Re = 250,000$. Hysteresis loop in the data for the aerodynamic coefficients was observed. Hysteresis has also been reported by Biber and Zumwalt [4] for a two-element GA(W)-2 airfoil and its extent was found to be a function of the angle of flap deployment, gap geometry and the history of changes in air speed or angle of attack. They also found that the hysteresis is not restricted to low Reynolds number

*Corresponding author.

E-mail address: smittal@iitk.ac.in (S. Mittal).

flows but can also be found at relatively high Reynolds number. The Reynolds number for their experiments is 2.2×10^6 . The present work is an effort to study the behavior of the flow past a NACA 0012 airfoil near stall by solving the governing flow equations numerically. Carefully conducted computations are utilized to track the hysteresis loop in the flow close to the stall angle.

The incompressible, Reynolds averaged Navier–Stokes (RANS) equations in conjunction with the Baldwin–Lomax model [3], for turbulence closure, are solved using stabilized finite element formulations. The finite element mesh consists of a structured mesh close to the body and an unstructured part, generated via Delaunay’s triangulation, away from the body. This type of a grid has the ability of handling fairly complex geometries while still providing the desired resolution close to the body to effectively capture the boundary layer flow, especially, in the context of unsteady flows. In addition, the structured grid around the body allows for efficient implementation of the turbulence model. Despite the simplicity of the Baldwin–Lomax model, its implementation with unstructured grids is quite complex. The interested reader is referred to the articles by Kallinderis [7], Mavriplis [8] and Anderson and Bonhaus [2] for details. For the relative performance of different turbulence models applied to geometries of aerospace interest the reader is referred to the review paper by Tulapurkara [15].

Stabilized finite element formulations are utilized to solve the flow equations in the primitive variables. Terms that are based on the element level integrals of the residuals, are added to the basic Galerkin formulation. These terms stabilize the computations against spurious numerical oscillations in advection dominated flows and enable the use equal-order-interpolation velocity–pressure elements. Since the stabilization terms are weighted residuals, the consistency of the formulation is maintained in the sense that the stabilized formulations still admits the exact solution. More details on the formulation can be found in the articles by Mittal [10] and Tezduyar et al. [13].

2. The governing equations

The spatial and temporal domains are denoted as $\Omega \subset \mathbb{R}^2$ and $(0, T)$, respectively. The spatial and temporal coordinates are denoted by \mathbf{x} and t and Γ represents the boundary of Ω . The Navier–Stokes equations governing incompressible fluid flow are

$$\rho \left(\frac{\partial \mathbf{u}}{\partial t} + \mathbf{u} \cdot \nabla \mathbf{u} - \mathbf{f} \right) - \nabla \cdot \boldsymbol{\sigma} = 0 \quad \text{on } \Omega \text{ for } (0, T), \quad (2.1)$$

$$\nabla \cdot \mathbf{u} = 0 \quad \text{on } \Omega \text{ for } (0, T). \quad (2.2)$$

Here ρ , \mathbf{u} , \mathbf{f} and $\boldsymbol{\sigma}$ are the density, velocity, body force and the stress tensor, respectively. The stress tensor is related to the velocity \mathbf{u} and pressure p by $\boldsymbol{\sigma} = -p\mathbf{I} + \mathbf{T}$ where $\mathbf{T} = 2\mu\boldsymbol{\varepsilon}(\mathbf{u})$. Here \mathbf{I} is the identity tensor, μ is the dynamic viscosity and $\boldsymbol{\varepsilon}(\mathbf{u}) = (1/2)((\nabla \mathbf{u}) + (\nabla \mathbf{u})^T)$. The boundary conditions are represented as $\mathbf{u} = \mathbf{g}$ on Γ_g and $\mathbf{n} \cdot \boldsymbol{\sigma} = \mathbf{h}$ on Γ_h where Γ_g and Γ_h are complementary subsets of the boundary Γ . The initial condition on the velocity is specified on Ω as $\mathbf{u}(\mathbf{x}, 0) = \mathbf{u}_0$ on Ω , where \mathbf{u}_0 is divergence free.

3. Finite element formulation

The domain Ω is discretized into subdomains Ω^e , $e = 1, 2, \dots, n_{el}$, where n_{el} is the number of elements. Let \mathcal{S}_u^h and \mathcal{S}_p^h be the appropriate finite element trial function spaces, and \mathcal{V}_u^h and \mathcal{V}_p^h the weighting function spaces for velocity and pressure. The stabilized finite element formulation of Eqs. (2.1) and (2.2) is written as follows: find $\mathbf{u}^h \in \mathcal{S}_u^h$ and $p^h \in \mathcal{S}_p^h$ such that $\forall \mathbf{w}^h \in \mathcal{V}_u^h, q^h \in \mathcal{V}_p^h$

$$\begin{aligned}
& \int_{\Omega} \mathbf{w}^h \cdot \rho \left(\frac{\partial \mathbf{u}^h}{\partial t} + \mathbf{u}^h \cdot \nabla \mathbf{u}^h - \mathbf{f} \right) d\Omega + \int_{\Omega} \boldsymbol{\varepsilon}(\mathbf{w}^h) : \boldsymbol{\sigma}(p^h, \mathbf{u}^h) d\Omega + \int_{\Omega} q^h \nabla \cdot \mathbf{u}^h d\Omega \\
& + \sum_{e=1}^{n_{el}} \int_{\Omega^e} \frac{1}{\rho} (\tau_{\text{SUPG}} \rho \mathbf{u}^h \cdot \nabla \mathbf{w}^h + \tau_{\text{PSPG}} \nabla q^h) \cdot \left[\rho \left(\frac{\partial \mathbf{u}^h}{\partial t} + \mathbf{u}^h \cdot \nabla \mathbf{u}^h - \mathbf{f} \right) - \nabla \cdot \boldsymbol{\sigma}(p^h, \mathbf{u}^h) \right] d\Omega^e \\
& + \sum_{e=1}^{n_{el}} \int_{\Omega^e} \delta \nabla \cdot \mathbf{w}^h \rho \nabla \cdot \mathbf{u}^h d\Omega^e = \int_{\Gamma_h} \mathbf{w}^h \cdot \mathbf{h}^h d\Gamma
\end{aligned} \tag{3.1}$$

The first three terms and the right-hand-side in the variational formulation given by Eq. (3.1) constitute the Galerkin formulation of the problem. The terms involving the element level integrals and the coefficients τ_{SUPG} and τ_{PSPG} are the stabilization terms added to the basic Galerkin formulation to enhance its numerical stability. These are based on the SUPG (streamline-upwind/Petrov–Galerkin) and PSPG (pressure-stabilizing/Petrov–Galerkin) method. Details on the formulation can be found in papers by Hughes and Brooks [6], Tezduyar et al. [13] and Mittal [10].

Equal-in-order basis functions for velocity and pressure, that are linear in space (three-noded triangular elements) are used. A three-point quadrature is employed for numerical integration. The time integration of the equations is carried out via the Generalized Trapezoidal rule. The non-linear, implicit, equation systems resulting from the finite-element discretization of the flow equations are solved using the generalized minimal residual technique [12] in conjunction with diagonal preconditioners. The formulation has been utilized, earlier, to solve a variety of unsteady flow problems (for example, see [11]).

4. Results and discussion

4.1. Boundary conditions

The NACA 0012 airfoil resides in a rectangular computational domain whose upstream and downstream boundaries are located at 5 and 11 chord lengths from the leading edge, respectively. The upper and lower boundaries are placed at 5 chord lengths, each, from the leading edge. The no-slip condition is specified for the velocity on the airfoil surface while free-stream values are assigned for the velocity at the upstream boundary. At the downstream boundary a Neumann type boundary condition for the velocity is specified that corresponds to zero viscous stress vector. On the upper and lower surface boundaries the component of velocity normal to the component of stress vector along these boundaries is prescribed zero value. The Reynolds number based on the chord length of the airfoil, free-stream velocity and viscosity of the fluid is 10^6 .

4.2. Finite element mesh and convergence

Fig. 1 shows a typical finite element mesh employed for the computations. This mesh consists of 19,071 nodes and 37,896 triangular elements. The unstructured mesh provides flexibility to handle complex geometries. The structured mesh around the airfoil provides effective control on the grid to resolve the boundary layer. In addition, it results in efficient computation of the eddy viscosity. Fig. 2 shows the pressure distribution on the airfoil surface for $\alpha = 15^\circ$. To establish convergence of the computations with respect to the spatial discretization, solution is also computed on a more refined mesh (mesh 2) with 41,263 nodes and 82,280 elements for $\alpha = 15^\circ$. The surface pressure distributions and the velocity profiles obtained from computations on the two meshes are shown in Figs. 2 and 3. It can be noticed that the two solutions are almost indistinguishable. The steady-state aerodynamic coefficients

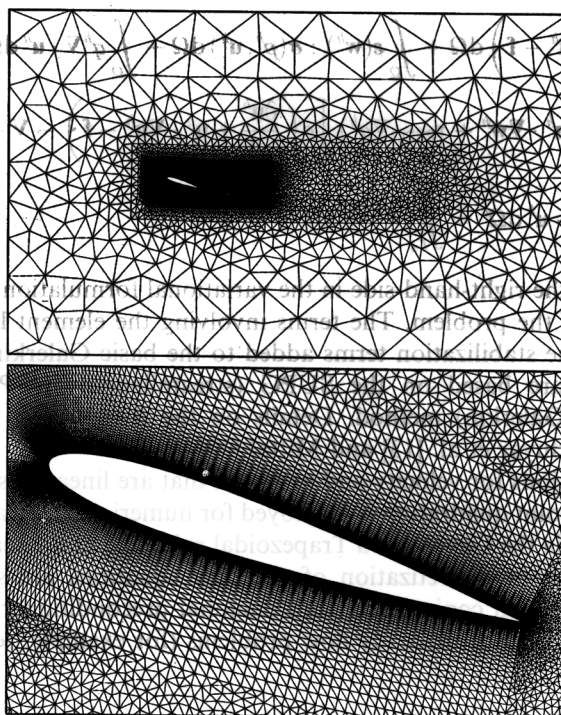


Fig. 1. Typical finite element mesh. The mesh shown is for $\alpha = 18^\circ$ and consists of 19,071 nodes and 37,896 elements.

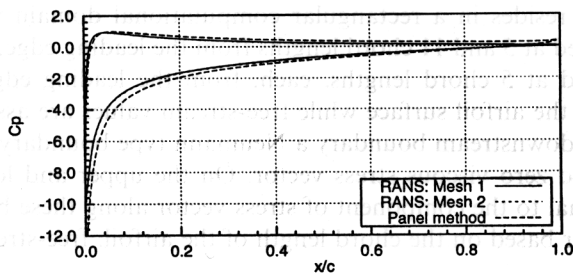


Fig. 2. $Re = 10^6$, $\alpha = 15^\circ$ turbulent flow past a NACA 0012 airfoil: C_p distribution on the airfoil surface. Also shown is the solution with the linear vortex panel method for the inviscid flow.

Fig. 1 shows a typical finite element mesh employed for the computations. The mesh consists of 19,071 nodes and 37,896 elements. The mesh is highly refined in the vicinity of the airfoil, particularly near the leading and trailing edges, to accurately capture the flow gradients. The mesh is structured to follow the airfoil's geometry, with a higher density of elements in the boundary layer region. The flow is simulated using a RANS approach with two different meshes (Mesh 1 and Mesh 2) and compared against a linear vortex panel method for inviscid flow. The results show that the viscous calculations are in close agreement with the inviscid solution, indicating that the mesh is sufficiently fine to resolve the flow structures.

for the two calculations differ by $<1\%$. This implies that mesh 1 is adequate to resolve the structures associated with these flow problems. Therefore, the rest of the computations reported in this article have been computed by utilizing meshes of similar resolution. Also shown in Fig. 2 is the pressure distribution obtained from the linear vortex panel method for the inviscid flow. Since the flow is attached for most of the part on the airfoil surface the pressure distribution from the viscous calculations is fairly close to that from the potential flow theory. It can also be seen that because of the difference in the pressure gradients the boundary layer on the lower surface of the airfoil is much thinner than that on the upper surface.

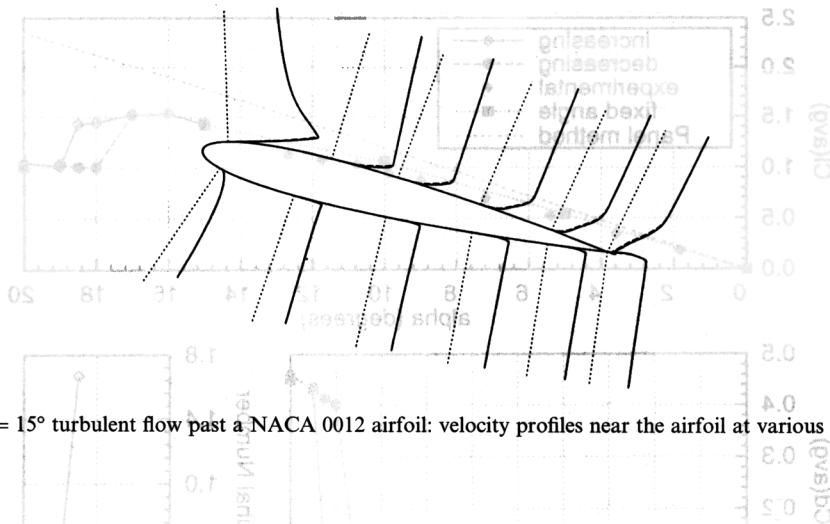


Fig. 3. $Re = 10^6$, $\alpha = 15^\circ$ turbulent flow past a NACA 0012 airfoil: velocity profiles near the airfoil at various stations. (---) mesh 1; (—) mesh 2.

4.3. Procedure of flow computation at various angles of attack

Computations for $\alpha = 0^\circ$, 5° , 10° and 15° are initiated with the steady state solution for $Re = 100$ at that angle of attack. The steady state solution is obtained by removing the unsteady terms from the governing equations. The Reynolds number is then ramped up to 10^6 over a period of, approximately, 500 time steps and the turbulence model is turned on. The computations are continued till the fully developed flow is obtained. These are referred to as *fixed* angle computations in the rest of the article. The fully developed solution for $\alpha = 15^\circ$ is used as an initial condition for computing the flow for $\alpha = 16^\circ$. The finite element mesh for this computation is obtained from the mesh for $\alpha = 15^\circ$ via a mesh-moving scheme that preserves the number of nodes and their connectivity. Once the fully developed flow for $\alpha = 16^\circ$ is obtained it is used as an initial condition to obtain the flow for $\alpha = 17^\circ$. The process continues till the fully developed flow for $\alpha = 20^\circ$ is computed. The series of solutions at various angles of attack, obtained by this method, approximates the situation where the wind-tunnel data for a static airfoil is collected by *increasing* the angle of attack in small increments. Next, the solution for $\alpha = 20^\circ$ is used as an initial condition to obtain the solution for $\alpha = 19^\circ$ which is in turn utilized to compute the flow for $\alpha = 18^\circ$ and so on. The solutions obtained in this manner will be referred to as the *decreasing* angle solutions.

4.4. Pre-stall flow regime

Fig. 4 shows the variation of the time-averaged values of the aerodynamic coefficients with the angle of attack for the computed solutions along with some experimental results from Thibert et al. [14]. The experimental results correspond to $Mach = 0.3$ and $Re = 1.8 \times 10^6$ flow. In the experiments the transition point was not fixed and no attempt was made to determine its location. However, the present computations do not model transition and the turbulence model is turned on right at the leading edge of the airfoil. Additionally, the flow is incompressible and the Reynolds number is a little lower than that in the experiments. This might explain some of the differences that can be noticed between the numerical and experimental results. Also shown in Fig. 4 are the lift coefficients obtained with the panel method. As expected, the estimates provided by the inviscid flow become poorer with increase in α and are completely unacceptable near the stall angle and beyond. Fig. 5 shows the flow fields for the steady-state solutions obtained at various angles of attack. The flow at 0° angle of attack is attached and symmetric about the airfoil chord, as expected. Mild separation, close to the trailing edge, can be observed at larger values of α .

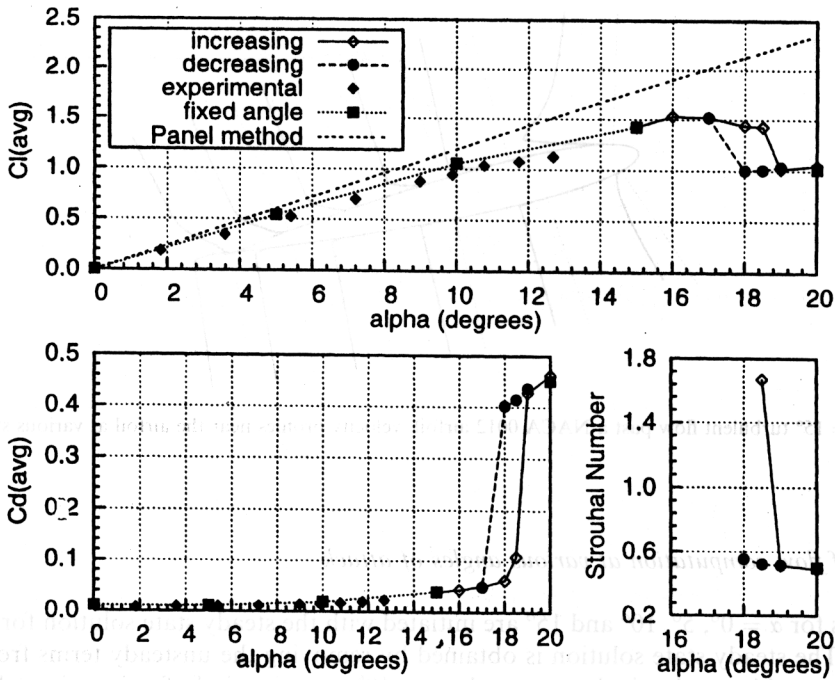


Fig. 4. $Re = 10^6$ turbulent flow past a NACA 0012 airfoil: variation of the time-averaged drag and lift coefficients and Strouhal number with angle of attack.

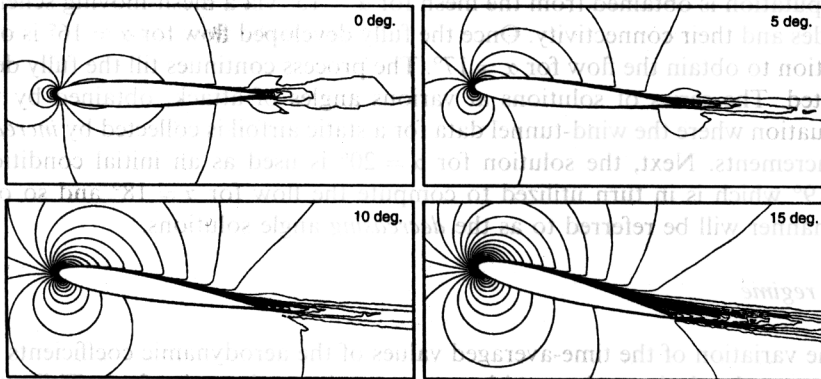


Fig. 5. $Re = 10^6$ turbulent flow past a NACA 0012 airfoil: magnitude of velocity for the steady-state solution at various angles of attack.

The separation point, on the upper surface of the airfoil, is located at $0.99c$ for $\alpha = 5^\circ$, $0.95c$ for $\alpha = 10^\circ$ and $0.64c$ for $\alpha = 15^\circ$. Here, c is the chord length of the airfoil.

4.5. Flow near the stall angle

At $\alpha = 17^\circ$ the fully developed flow achieves a steady state. The time histories of the lift and drag coefficients are shown in Fig. 6. After an initial transient, steady-state values are attained for $\alpha = 17^\circ$. Note

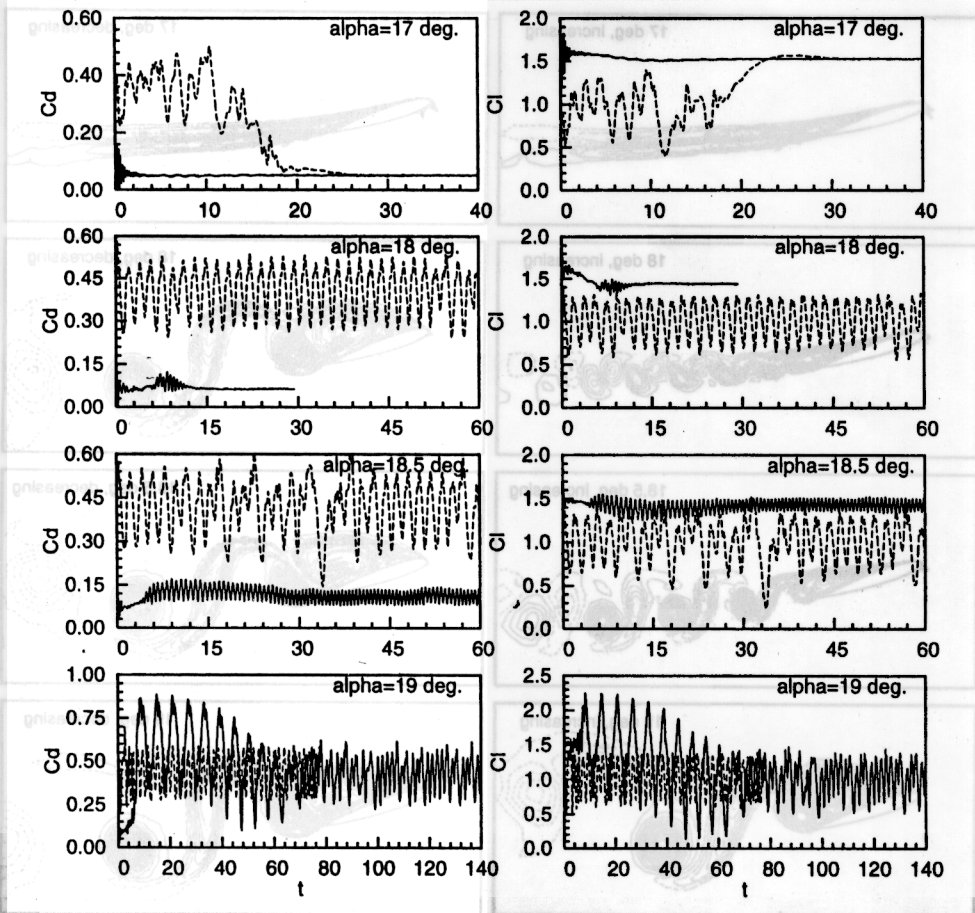


Fig. 6. $Re = 10^6$ turbulent flow past a NACA 0012 airfoil: time histories of the drag and lift coefficients: (---) decreasing angle; (—) increasing angle.

that the steady-state solutions obtained from the increasing and decreasing α are identical. This is also reflected in the vorticity fields shown in Fig. 7.

On increasing α from 17° to 18° , the solution becomes unsteady and remains so at larger angles of attack. The solution obtained with the increasing angle is associated with significantly less unsteadiness compared to that computed with decreasing angle. For the flow obtained with increasing angle the vortex shedding takes place at close to the trailing edge of the airfoil. For this reason, the effect of shedding on the time histories of the aerodynamic coefficients is hardly perceptible and the values are almost constant in time. On the other hand, for the solution corresponding to the decreasing angle, the flow separates right at the leading edge and unsteadiness in the flow is quite large. This results in fairly large variations in the drag and lift coefficients and can be observed in the time histories shown in Fig. 6. The longitudinal spacing between the vortices in a wake is intimately related to the vortex shedding frequency. From Fig. 7 it is seen that this spacing is larger for the decreasing angle solution.

The difference between the increasing and decreasing angle solutions is also observed at $\alpha = 18.5^\circ$. For the increasing angle, the unsteadiness in the solution increases with angle of attack. The magnitude of the unsteady component in the time variation of the aerodynamic coefficients (see Fig. 6) is larger for $\alpha = 18.5^\circ$

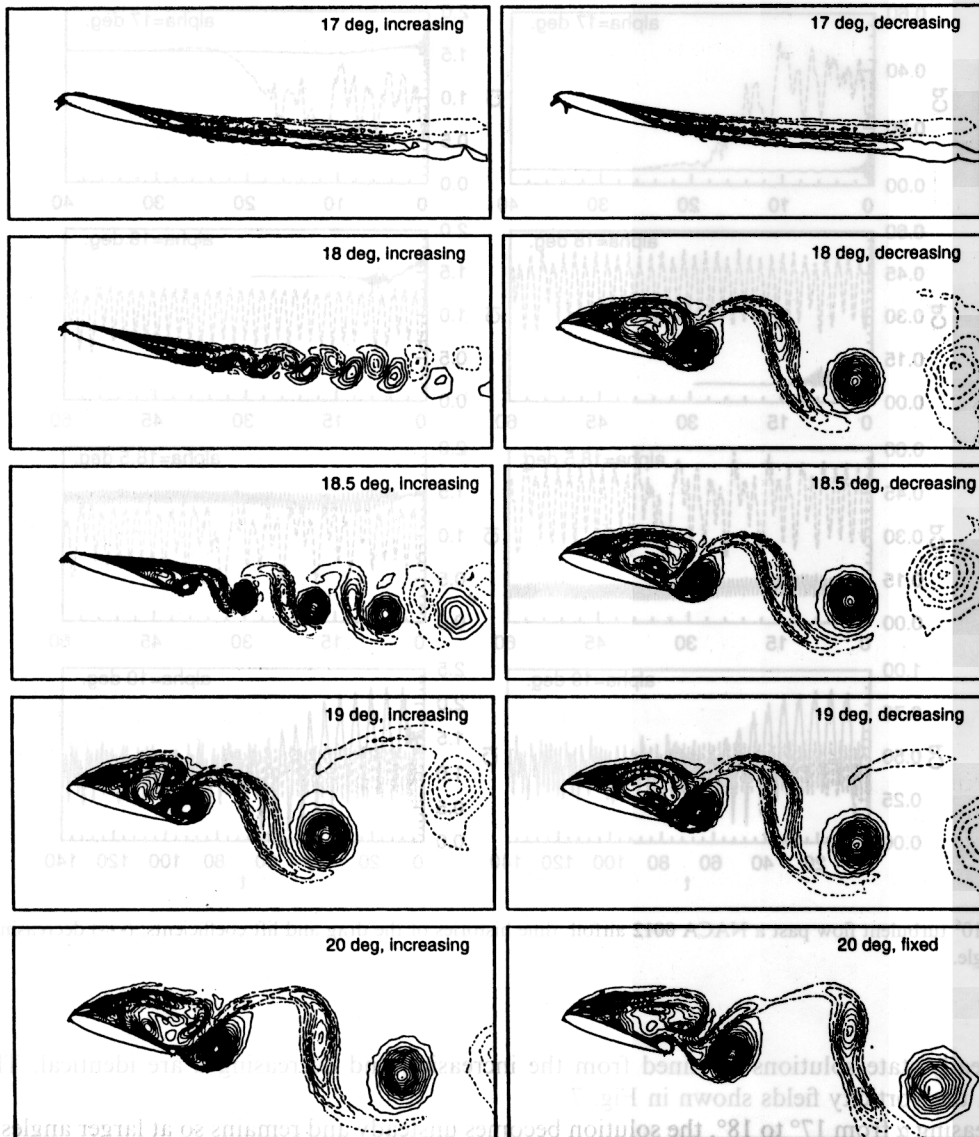


Fig. 7. $Re = 10^6$ turbulent flow past a NACA 0012 airfoil: vorticity field at various angles of attack for the fully developed flow at a time instant corresponding to the maximum lift coefficient. The left column shows the solution for increasing angle while the right ones for the decreasing angle. The solution in the right bottom corner for $\alpha = 20^\circ$ has been computed by keeping the same α since the beginning of the simulation. (---) clockwise vorticity; (—) counter-clockwise vorticity.

compared to that at $\alpha = 18^\circ$. However, for the decreasing angle, the level of unsteadiness is virtually the same for angles of attack 18° and beyond. In fact, the solutions for $\alpha = 18^\circ$ and 18.5° are quite comparable to each other.

From the time histories of the aerodynamic coefficients for $\alpha = 19^\circ$, in Fig. 6, it is seen that although the transient behavior of the two solutions is quite different they eventually develop to the same unsteady solution. The vorticity fields for the fully developed solutions, in the two cases as shown in Fig. 7 are very

similar. Similarly, at $\alpha = 20^\circ$ it is found that the solutions obtained by increasing the angle and that obtained by initiating the computations from the steady-state flow at $Re = 100$ are same. The vorticity fields shown in Fig. 7 confirm this observation.

4.6. Hysteresis in the flow

Hysteresis in the flow is observed for $17^\circ < \alpha < 19^\circ$. It can be seen from the variation of the mean aerodynamic coefficients with angle of attack, their time histories and the vorticity fields shown in Figs. 4, 6 and 7, respectively.

Flow at low angles of attack, for example, at $\alpha = 0^\circ$ and 5° is completely attached on, both, the lower and upper surfaces of the airfoil. At larger angles of attack the flow, on the upper surface, begins to separate near the trailing edge of the airfoil. The separation point moves towards the leading edge as the angle of attack increases. At $\alpha = 10^\circ$ the flow separates at $0.95c$ from the leading edge. The location of the separation point with respect to the leading edge is, approximately, $0.64c$ for $\alpha = 15^\circ$, $0.52c$ for $\alpha = 16^\circ$, $0.38c$ for $\alpha = 17^\circ$, $0.25c$ for $\alpha = 18^\circ$ and $0.09c$ for $\alpha = 18.5^\circ$. At $\alpha = 19^\circ$ the separation point moves right up to the leading edge and stall is observed. This is consistent with the well-known observation that a trailing edge stall is observed for thick airfoils. For the decreasing angle, the flow seems to remember its past history and the separation point is located at the leading edge for all $\alpha \geq 18^\circ$. For this branch of the solution, stall is observed at $\alpha = 17^\circ$. The solutions for $\alpha = 19^\circ, 20^\circ$ for the increasing angle and $\alpha = 19^\circ, 18.5^\circ$ and 18° for the decreasing angle and for $\alpha = 20^\circ$ for the fixed angle are all quite similar. In all the cases the flow separates right at the leading edge.

Fig. 8 shows the velocity profiles for the solutions with the increasing and decreasing angles for $\alpha = 18^\circ$. The difference in the separation points for the two solutions is clearly seen in this figure. The velocity profiles on the lower surface of the airfoil are also different in the two cases. This is, perhaps, caused by the difference in the location of the stagnation point for the two flows.

Measurements of Abott and von Doenhoff [1] indicate that the NACA 0012 airfoil stalls at $\alpha = 16^\circ$. The $(C_L)_{\max}$ reported by them is, approximately, 1.5. Our computations result in the same value of $(C_L)_{\max}$. The stall angle is found to be 17° for the computations with decreasing angle. This is a slight overprediction compared to the measured value. Qualitatively, the hysteresis loop resembles the one reported by Hoffmann [5] for his experiments with the NACA 0015 airfoil for low values of free stream turbulence (FST). He found that with low FST ($=0.25\%$) the airfoil stalls at, approximately, 25° for the increasing angle of attack and at 18° for the decreasing angle.

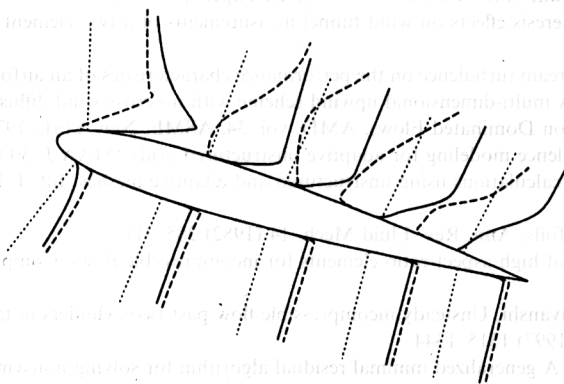


Fig. 8. $Re = 10^6$, $\alpha = 18^\circ$ turbulent flow past a NACA 0012 airfoil: velocity profiles near the airfoil at various stations for the solutions with decreasing and increasing angle. (---) decreasing angle; (—) increasing angle.

In addition to the difference in the flow structure, the mean and unsteady components of the aerodynamic coefficients for the two solutions associated with the hysteresis loop are also quite different. This suggests that close to the stall angle measurements should be made carefully and they can depend on the history of how the flow is established in a wind tunnel.

5. Conclusions

Results have been presented for computation of flow past a NACA 0012 airfoil using RANS equations in conjunction with a Baldwin–Lomax turbulence model for closure. A stabilized finite element method has been utilized to solve the incompressible Navier–Stokes equations in the primitive variables formulation. Computations have been carried out for progressively increasing and decreasing angles of attack. Hysteresis in the flow has been observed close to the stall. With the increasing angle of attack, stall occurs at 19° while for the decreasing angle it occurs at 17° . The ability of the flow to remember its past history is responsible for its hysteretic behavior. Close to the stall the movement of the separation point with angle of attack is relatively slow with the increasing angle while it is quite abrupt with the decreasing angle. For the same angle of attack, in the hysteresis loop, the flow obtained with the *decreasing* angle of attack is associated with larger unsteadiness, lower lift and higher drag while the one with *increasing* angle results in higher lift and lower drag.

Acknowledgement

Partial support for this work from the Aeronautical Research & Development Board, India is gratefully acknowledged.

References

- [1] J.H. Abott, A.E. von Doenhoff, Theory of Wing Sections, Dover, New York, 1959.
- [2] W.K. Anderson, D.L. Bonhaus, An implicit upwind algorithm for computing turbulent flows on unstructured grids, *Computers Fluids* 23 (1994) 1–21.
- [3] B. Baldwin, H. Lomax, Thin layer approximation and algebraic turbulence model for separated turbulent flows, AIAA 16th Aerospace Sciences Meeting, Huntsville, Alabama, 1978, AIAA Paper, pp. 78–257.
- [4] K. Biber, G.W. Zumwalt, Hysteresis effects on wind tunnel measurements of a two-element airfoil, *AIAA J.* 31 (2) (1993) 326–330.
- [5] J.A. Hoffmann, Effects of freestream turbulence on the performance characteristics of an airfoil, *AIAA J.* 29 (9) (1991) 1353–1354.
- [6] T.J.R. Hughes, A.N. Brooks, A multi-dimensional upwind scheme with no cross-wind diffusion, in: T.J.R. Hughes (Ed.), *Finite Element Methods for Convection Dominated Flows*, AMD, vol. 34, ASME, New York, 1979, pp. 19–35.
- [7] Y. Kallinderis, Algebraic turbulence modeling for adaptive unstructured grids, *AIAA J.* 30 (1992) 631–639.
- [8] D.J. Mavriplis, Turbulent flow calculations using unstructured and adaptive meshes, *Int. J. Num. Meth. Fluids* 13 (1991) 1131–1152.
- [9] W.J. McCroskey, Unsteady airfoils, *Ann. Rev. Fluid Mech.* 14 (1982) 285–311.
- [10] S. Mittal, On the performance of high aspect-ratio elements for incompressible flows, *Computer Meth. Appl. Mech. Engrg.* 188 (2000) 269–287.
- [11] S. Mittal, V. Kumar, A. Raghuvanshi, Unsteady incompressible flow past two cylinders in tandem and staggered arrangements, *Int. J. Num. Meth. Fluids* 25 (1997) 1315–1344.
- [12] Y. Saad, M. Schultz, GMRES: A generalized minimal residual algorithm for solving nonsymmetric linear systems, *SIAM J. Sci. Stat. Comp.* 7 (1986) 856–869.
- [13] T.E. Tezduyar, S. Mittal, S.E. Ray, R. Shih, Incompressible flow computations with stabilized bilinear and linear equal-order-interpolation velocity-pressure elements, *Computer Meth. Appl. Mech. Engrg.* 95 (1992) 221–242.

- [14] J.J. Thibert, M. Grandjacques, L.H. Ohman, Experimental database for computer program assessment, TR AR-138, AGARD.
- [15] E.G. Tulapurkara, Turbulence models for the computation of flow past airplanes, *Prog. Aero. Sci.* 33 (1997) 71–165.